ADVANCES IN ATMOSPHERIC SCIENCES, VOL. 32, MAY 2015, 659–670

Seasonal Variation and Physical Properties of the Cloud System over Southeastern China Derived from CloudSat Products

GUO Zhun[1,2] and ZHOU Tianjun*[1,3]

[1] *State Key Laboratory of Numerical Modeling for Atmospheric Sciences and Geophysical Fluid Dynamics,*
Institute of Atmospheric Physics, Chinese Academy of Sciences, Beijing 100029
[2] *Climate Change Research Center, Chinese Academy of Sciences, Beijing* 100029
[3] *Joint Center for Global Change Studies, Beijing* 100875

(Received 2 April 2014; revised 9 August 2014; accepted 15 September 2014)

ABSTRACT

Based on the National Centers for Environmental Prediction (NCEP) and Climate Prediction Center (CPC) Merged Analysis of Precipitation (CMAP) data and CloudSat products, the seasonal variations of the cloud properties, vertical occurrence frequency, and ice water content of clouds over southeastern China were investigated in this study. In the CloudSat data, a significant alternation in high or low cloud patterns was observed from winter to summer over southeastern China. It was found that the East Asian Summer Monsoon (EASM) circulation and its transport of moisture leads to a conditional instability, which benefits the local upward motion in summer, and thereby results in an increased amount of high cloud. The deep convective cloud centers were found to coincide well with the northward march of the EASM, while cirrus lagged slightly behind the convection center and coincided well with the outflow and meridional wind divergence of the EASM. Analysis of the radiative heating rates revealed that both the plentiful summer moisture and higher clouds are effective in destabilizing the atmosphere. Moreover, clouds heat the mid-troposphere and the cloud radiative heating is balanced by adiabatic cooling through upward motion, which causes meridional wind by the Sverdrup balance. The cloud heating–forced circulation was observed to coincide well with the EASM circulation, serving as a positive effect on EASM circulation.

Key words: East Asian summer monsoon, seasonal cycle, CloudSat, cloud

Citation: Guo, Z., and T. J. Zhou, 2015: Seasonal variation and physical properties of the cloud system over southeastern China derived from CloudSat products. *Adv. Atmos. Sci.*, **32**(5), 659–670, doi: 10.1007/s00376-014-4070-y.

1. Introduction

Clouds play a vital role in the earth's climate system because of their influence on radiative heating. The distribution of clouds has a profound impact on radiative energy balance, which is the main driver for atmospheric circulations and climate systems (Hartmann et al., 1992). Therefore, studies on the changes in cloud distributions, radiative effect, and their formation mechanisms are of essential importance to our understanding of climate changes.

The formation mechanism of cloud types is associated with the dynamic and thermal conditions (Houze, 1994). The radiative effects and feedback of clouds depend on their properties (Arking, 1991; Hartmann et al., 1992). Low stratiform cloud, such as marine boundary layer cloud, corresponds to lower troposphere static stability and has a strong net radiative cooling effect on the atmosphere (Klein and Hartmann, 1993; Lin et al., 2009). Some studies have demonstrated that there is positive feedback between SST and stratiform cloud over the northern Pacific and the oceans of the eastern tropics (Norris and Leovy, 1994; Huang and Hu, 2007). On the contrary, high clouds, such as deep convective and cirrus clouds, have a cancellation effect on long- and short-wave cloud radiative forcing (CRF), regulating the SST of the western Pacific warm pool (Ramanathan and Collins, 1991), except in El Niño years (Cess et al., 2001).

Southeastern China is covered by a large amount of cloud (Wang et al., 2004), and is also one of the most significant stratiform cloud regions (Klein and Hartmann, 1993). Therefore, this region has a strong net radiative cooling effect (Rajeevan and Sriviasan, 2000; Wang et al., 2004). Moreover, this region also has a significant annual cycle in cloud cover that the high- and low- cloud alternates with each other (Yu et al., 2001; Luo et al., 2009). However, because of the limitation of conventional cloud data and the complexity of cloud physics, knowledge about the formation mechanisms and climate effects of cloud in this region is still limited. Only a limited number of studies exist that have focused on the effects of total cloud amounts on the East Asian summer monsoon (EASM).

The climate of southeastern China is dominated by the activity of the EASM (Wang et al., 2004; Ding and Chan, 2005; Zhou et al., 2009a), whose onset is a key indicator

---

* Corresponding author: ZHOU Tianjun
Email: zhoutj@lasg.iap.ac.cn

characterizing the abrupt transition from the dry to the rainy season and the subsequent seasonal march (Ding and Chan, 2005). Therefore, both the onset and march of the EASM further influence the properties of clouds by changing the atmospheric conditions. Recently, the availability of CloudSat (a new satellite-based cloud experiment; Stephens et al., 2002), for which the satellite was launched in 2006 as part of National Aeronautics and Space Administration (NASA)'s A-Train constellation of satellites (L'Ecuyer and Jiang, 2010), has provided us with an opportunity to reveal vertically-resolved cloud properties and formation mechanisms.

The primary purpose of this study is to investigate the relationship between the variations of cloud properties and EASM circulation over southeastern China. In addition, we also want to address the following questions: (1) What are the seasonal variations of cloud properties derived from CloudSat data? (2) What is the influence of EASM circulation on the vertical structure of cloud properties? (3) What kind of interaction occurs between cloud (their heating effects) and EASM circulation?

The remainder of the paper is organized as follows. The data and methodology are described in section 2. The seasonal variation of the cloud properties over southeastern China and the large-scale triggers for the prevailing cloud types are analyzed in section 3. The seasonal meridional migration of the cloud system and its vertical structures associated with the advance and retreat of the EASM are analyzed in section 4. Section 5 presents an analysis of the radiative heating rates of the clouds. The major findings are summarized in section 6.

2. Data and methods

2.1. *Satellite data*

To analyze the cloud profiles over southeastern China, five standard data products from CloudSat version 4, namely 2B-GEOPROF, 2B-GEOPROF-lidar, 2B-CWC-RO, 2B-CLDCLASS and 2B-FLXHR, were used (http://www.cloudsat.cira.colostate.edu/dataSpecs.php). The CloudSat is an active remote sensor, which is useful for the observation of the vertical locations of hydrometeor layers (Mace, 2007). The Cloud Profiling Radar (CPR) mounted on the CloudSat satellite identifies the radar echoes from hydrometeors and produces an estimate of the radar reflectivity factor for each volume deemed to contain significant echo (Stephens et al., 2002).

The 2B-GEOPROF product determines the existence of clouds by examining the CloudSat CPR radar echo, and then compares with the Moderate Resolution Imaging Spectroradiometer (MODIS) cloud mask spectral tests. Finally, the geometrical profile of clouds is obtained, which includes cloud mask, cloud fraction, radar reflectivity, and gaseous attenuation (Mace et al., 2007).

The 2B-GEOPROF-lidar data is the product of a combination of both CPR and CALIPSO (the Cloud-Aerosol Lidar and Infrared Pathfinder Satellite Observation) Cloud-Aerosol Lidar with Orthogonal Polarization (CALIOP). The CPR can probe optically thick large particle layers, while CALIOP can probe optically thin layers and tenuous cloud tops. An efficient cooperation of the two instruments can provide more reliable and accurate geometrical profiles of cloud (Mace, 2007).

The 2B-CLASS product classifies the clouds into eight types by examining the maximum effective radar reflectivity, precipitation, temperature, and vertical scale of hydrometeors. It includes cirrus, altostratus, altocumulus, stratus, stratocumulus, cumulus, nimbostratus, and deep convection clouds (Wang and Sassen, 2007).

The 2B-FLXHR product uses the liquid and ice water content estimated from the CPR and European Centre for Medium-Range Weather Forecasts (ECWMF) reanalysis to produce the estimates of broadband fluxes and heating rates for each radar profile (L'Ecuyer et al., 2008).

In this study, all the CloudSat datasets span from June 2006 to June 2010. The data are interpolated onto a grid with $1^\circ \times 1^\circ$ resolution. The products (i.e. cloud properties) are derived from satellite tracks. There are about 14 tracks in a day and about 420 tracks in a month. The frequency and corresponding satellite products are counted when the satellite flies over an assumed grid box. And then, for each grid and each month, such a treatment allows sufficient sampling for meaningful use. There are at least 4000 valid samples in each grid and each month. The monthly averaged products are the average of all those 4000 samples.

Similar to Xi et al. (2010), the occurrence frequency of cloud is defined by using cloud mask derived from 2B-GEOPROF. The cloud mask is 0 for clear sky and 100% when cloud mask is lager than 20. When cloud mask is less than 20, the cloud occurrence frequency is set to the cloud fraction, which is derived from 2B-GEOPROF-lidar. Therefore, the cloud occurrence frequency is a ratio of the number of times when the cloud mask is larger than 20 to the total number of satellite observations.

2.2. *Reanalysis data and precipitation data*

The atmospheric general circulation data are from the National Centers for Environmental Prediction (NCEP) Department of Energy (DOE) Atmospheric Model Intercomparison Project (AMIP) reanalysis (hereafter NCEP2) (Kanamitsu et al., 2002). In addition, Climate Prediction Center (CPC) Merged Analysis of Precipitation (CMAP) precipitation data are also used to describe the monsoon rain band (Xie and Arkin, 1996). Corresponding to the CloudSat data, the time periods of NCEP2 and CMAP also range from June 2006 to June 2010.

3. The seasonal variation of cloud properties over southeastern China

3.1. *The seasonal variation of cloud properties derived from CloudSat data*

To demonstrate the seasonal cycle of cloud properties, the occurrence frequencies of five cloud types derived from

CloudSat data are presented in Fig. 1. It can be observed that there are more stratiform clouds, especially stratocumulus, in winter than in summer. In contrast, high clouds are prevalent in summer, especially cirrus and deep convective clouds. The cloud properties derived from CloudSat data are slightly different from those derived from the International Satellite Cloud Climatology Project (ISCCP_D2). The dominant cloud type over southeastern China is noted to be nimbostratus in ISCCP-D2 data (Yu et al., 2004), but stratocumulus in CloudSat data (Fig. 1). This difference is due to the different methods of categorizing cloud types in the ISCCP and CloudSat datasets. The categories of clouds in CloudSat are defined by their horizontal and vertical cloud dimensions, base height, precipitation, and water path (Sassen and Wang, 2008); however, in ISCCP, the categories are just defined by visible spectrometry (or infrared) cloud-top pressure and optical depth data (Rossow and Schiffer, 1991; Wang and Sassen, 2001; Sassen and Wang, 2008). Although the prevalent winter cloud types derived from the two datasets are different, they are highly consistent in measuring the seasonal variation of cirrus; both reach their maximum values in summer.

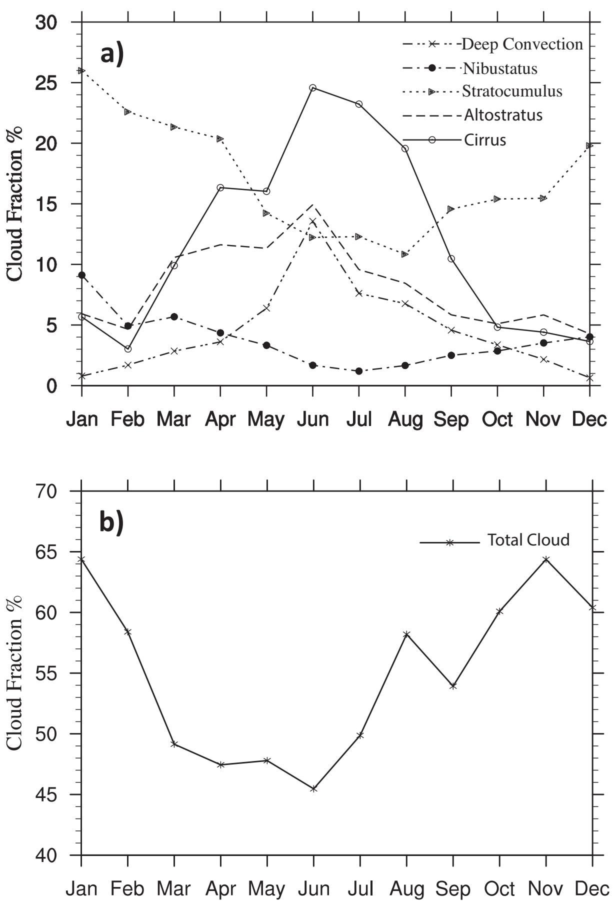

Fig. 1. The (a) vertical mean cloud occurrence frequency of five types and (b) total cloud occurrence frequency averaged in the region (22°–32°N, 105°–120°E).

3.2. *Large-scale circulation triggers for the seasonal change of prevailing cloud types over southeastern China*

The mean vertical profiles of horizontal divergence and vertical velocity are shown in Fig. 2. The wintertime low-level convergence and mid-level divergence prohibit deep convection, and thus high clouds cannot form. As a result, the wintertime upward motion is shallow and peaks at around 2 km (Fig. 2b). Such a kind of vertical profile of horizontal divergence is caused by the blocking and frictional effects of the Tibetan Plateau (Yu et al., 2004).

In boreal summer, the low-level convergence is still evident, but the mid-level divergence is replaced by a convergence, along with a high-level divergence (Fig. 2a), indicating the impact of the EASM. A deep convection peaking at 6 km is also evident. The strong upward motion enhances the updraft of mass flux, which is in favor of the increase in the occurrence frequency of high clouds, such as deep convective and cirrus clouds (Fig. 1).

To gain further information on the general circulation, the potential and equivalent potential temperature (θ and θ_e) averaged over southeastern China are calculated using the NCEP2 data (Fig. 3a). Lower troposphere stability (LTS), which is defined as $\theta_{700\ \mathrm{hPa}} - \theta_{1000\ \mathrm{hPa}}$, is correlated with the occurrence frequency of stratiform clouds, both seasonally and geographically (Klein and Hartmann, 1993). Over southeastern China, the season with the maximum stratiform cloud is associated with the largest LTS. In boreal winter, this region is highly stable, having an LTS value of 18.6 K (Fig. 3b). Owing to the dynamic effects of the Tibetan Plateau (Yu et al., 2004), the convections are restricted to the lower troposphere, which is in favor of the formation of a large amount of stratiform clouds in winter.

In boreal summer, the LTS falls to its minimum value (14.0 K), which is associated with a weaker inversion. This tends to result in a poorly-mixed, strong entraining boundary layer, where there is efficient turbulent decoupling of the cloud layer with the sub-cloud layer, and the surface moisture supply is cut off. Following the strong solar radiation input in summer, the entrainment at the stratiform cloud-top is enhanced. Associated with the strong evaporation caused by a warm cloud-base, the occurrence frequency of stratiform clouds sharply decreases in summer.

The seasonal cycle of total cloud is different from that of stratiform cloud. The high cloud occurrence frequency reaches its peak in boreal summer over southeastern China due to the contribution of increased high clouds. Figure 3 shows that the summertime equivalent potential temperature decreases vertically with height from 0 to 4 km, but increases with height from 4 km up to the TOA. Furthermore, a strong negative correlation between high cloudiness and lower-troposphere conditional stability is found (Fig. 3b). These features reflect the impact of EASM moisture transports, when the summer monsoon circulation replaces the Hadley cell over southeastern China (Ye and Yang, 1979; Zhou and Li, 2002; Chen et al., 2010). The strong upward

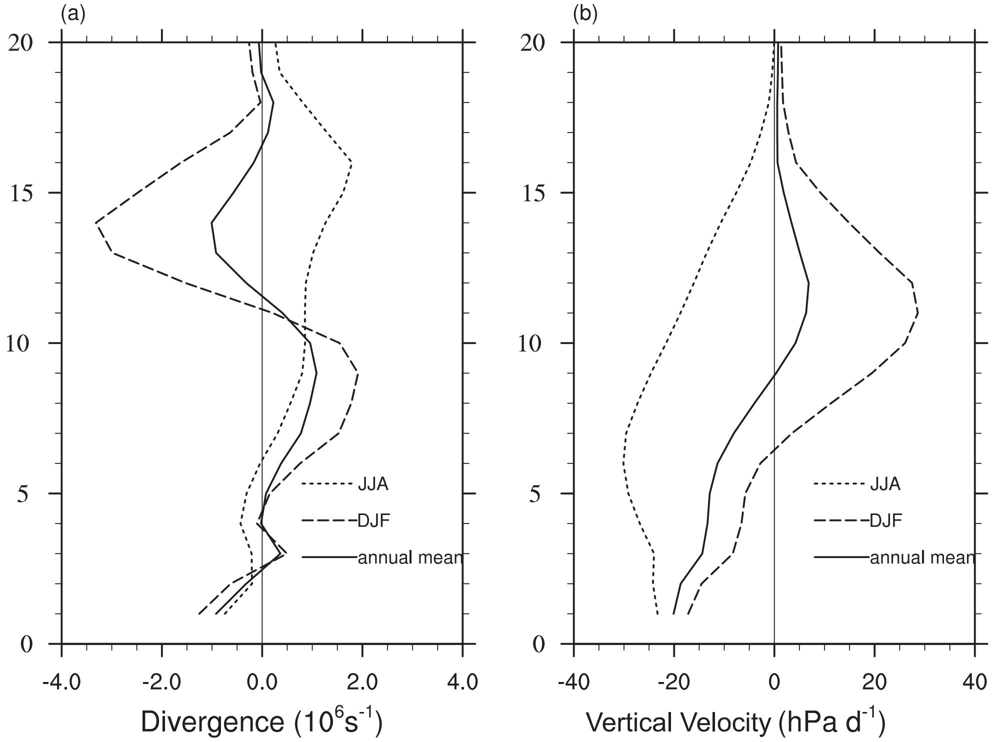

Fig. 2. The 2006–2010 mean vertical profile of horizontal divergence and vertical velocity averaged within the region (22°–32°N, 105°–120°E). The vertical coordinate is the height (units: km).

motion determines the height and occurrence frequency of the high cloud, as well as plays a critical role in the vertical transport of water vapor.

4. Advance and retreat of the EASM cloud system and its vertical structures

The above discussion already shows that the EASM plays an essential role in the seasonal variation of the vertical structure of clouds by changing the atmospheric circulations over southeastern China. The seasonal variations of the vertical structure of clouds also reflects the advance and retreat of the EASM. The seasonal movement of the rain belt is the most significant indicator of monsoon advance and retreat (Zhou and Li, 2002; Ding and Chan, 2005; Chen et al., 2010). In the following discussion, we depict the seasonal march of the monsoon by the maximum value of mean precipitation over southeastern China (105°–120°E).

The monthly evolution of vertical–latitude profiles of cloud occurrence frequency zonally averaged between 105°E and 120°E is shown in Fig. 4 (upper colored part of each panel). To clearly describe the relationship between cloud system formations and monsoon circulation movement, the corresponding meridional and vertical winds are also shown, and the precipitation averaged over the same longitudes at each month are displayed in the lower part of each panel. It is clear that the frequent cloud occurrence is well synchronized with the rain belts, as well as the EASM upwelling (Fig. 4). It can be observed that a front-like cloud structure, whose base coincides well with the rain belts, tilts northward with altitude (Figs. 4a and b). Following the seasonal march of the summer monsoon circulation, the frequent cloud occurrence indicated by the front-like cloud structure and rain belt move northward consistently.

From Figs. 5a and b it can be seen that, before the summer monsoon season, the precipitation center is located in South China around 25°N. The front-like cloud structure, with its base located at 25°N, where the northward warmer air encounters the southward colder air, is attributed to the quasi-stationary fronts that prevail in spring and winter. Above 11 km, there is no cloud from 20°N to higher latitudes. Following the seasonal progression of the EASM, the tropical convective systems gradually expand northward.

In June, the vertical monsoon circulation establishes over southeastern China and the center of high clouds over the South China Sea extends northward to the continent (Fig. 4c). The occurrence frequency of high clouds over southeastern China increases in magnitude and the dip of the frequent belt moves upward to a higher level. An increase is also seen in the amount of precipitation. As will be shown later, a predominant increase in the cloud occurrence frequency of cirrus and deep convective clouds is observed, with the latter being associated with precipitation.

Following the consecutive northward advance of summer monsoon in July, both the rain belt and frequent cloud center under 11 km arrive at their northernmost position, and the high-level frequent cloud center above 11 km expands northward (Fig. 4d). It is clear that when the monsoon

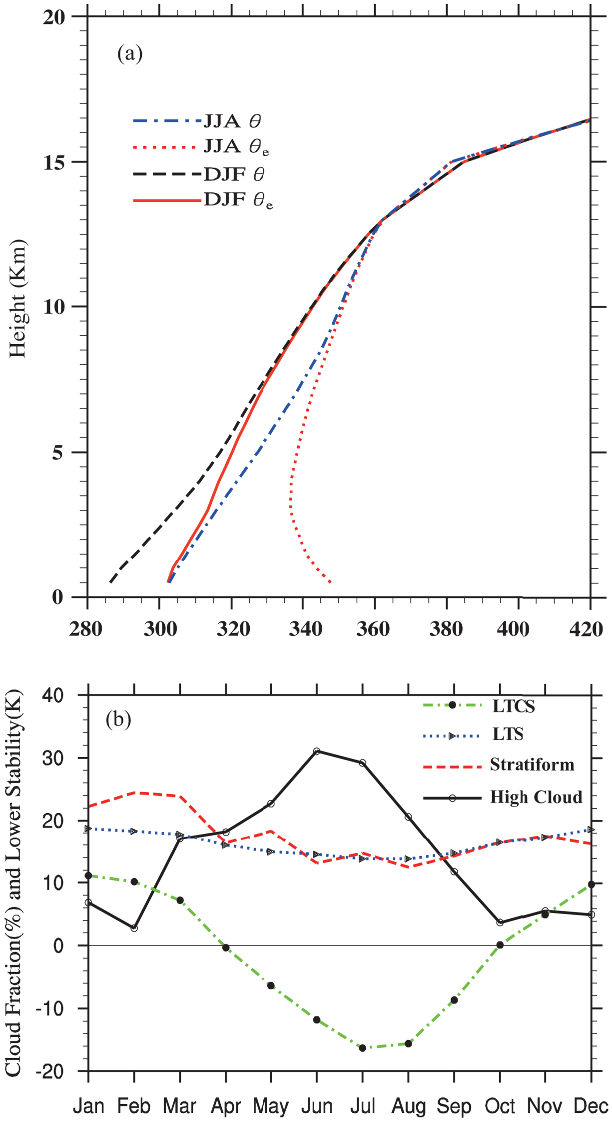

Fig. 3. The (a) vertical profiles of potential and equivalent potential temperature (θ and θ_e, units: K) in DJF (December–January–February) and JJA (June–July–August) averaged over southeastern China and (b) seasonal cycle of high cloudiness, stratocumulus, lower troposphere stability (LTS), and lower troposphere conditional stability (LTCS).

circulation is fully established, the maximum cloud occurrence frequency below 11 km coincides well with the vertical monsoon circulation. In the meantime, the high-level cloud center above 10 km lags behind the upwelling monsoon circulation, indicating that the outflow of convection is accompanied by frequent convective anvil clouds and divergence (Figs. 4c and d).

From April to July, although the northward movement of the cloud system is consistent with the northward progress of monsoon circulation, the maximum cloud occurrence frequency below 11 km is found to lead the monsoon rain belt slightly (Figs. 4a–d).

After August, following the southward retreat of the summer monsoon, both the cloud system and rain belt withdraw southward abruptly. The upper-level occurrence frequency center above 11 km almost disappears, and the front-like cloud system dominates South China again (Figs. 4e and f).

Following the northward movement of the monsoon circulation and associated cloud system, the cloud ice water content (IWC) is observed to show a similar seasonal march (Fig. 6). The consistent northward movement of the front-like cloud system and the outflow of convection are also evident in the structures of IWC.

The increase in IWC following the monsoon's progress is found to be consistent with the uplift of the cloud-top caused by an enhanced upwelling of monsoon circulation. Owing to the latitude-dependence of the tropopause, the altitude of IWC is observed to decrease with latitude (Fig. 5).

The above evidence shows that the seasonal advance of the monsoon circulation determines the seasonal cycle of the cloud properties over southeastern China. The cloud system as a whole may contain several types of clouds. To demonstrate this, we analyze the occurrence frequency of deep convective clouds, altostratus, and cirrus. All of them show significant seasonal variations with their peaks in boreal summer.

The maximum frequency of deep convective clouds partly represents the strength of deep convective systems, because its seasonal cycle agrees well with that of the upward motion and precipitation (Fig. 6). Both the frequency and horizontal span of deep convective clouds are determined by the monsoon circulation. In boreal summer, the contribution of deep convective clouds to total cloud occurrence frequency has been found to exceed 50% in the lower and middle troposphere. Following the advance and retreat of monsoon circulation, the center of deep convective clouds has also been observed to exhibit a similar meridional movement. In addition, following the dominance of upward monsoon circulation over southeastern China in June, the frequency of convective cloud has also been noted to reach its peak (Fig. 6c). In July, the center of convective cloud has been found to reach its northernmost latitude, 35°N (Fig. 6d).

Cirrus is also evident over southeastern China. Figure 7 displays the occurrence frequency of cirrus. In the ice cloud layer above 10 km, cirrus dominates the total cloud. The occurrence frequency of cirrus is generally higher than deep convection clouds. The center of the cirrus cloud slightly lags behind the deep convective systems, as evidenced by the center of the deep convective cloud and the rain belt. Unlike cirrus, the altostratus is located in front of deep convections in the mid-level (5–10 km). Above the convective clouds, the occurrence frequency of altostratus is extremely low (figure omitted).

In summary, when the summer monsoon circulation is fully established over southeastern China, the deep convective cloud is collocated with the upwelling circulation, whose central position is the same as the maximum cloudy-sky radiative heating (Fig. 8). Both the cloud anvil and cirrus are coupled with the convective detrainment and divergent outflow of monsoon circulation in upper levels. They also spread outward from the center of convections. Owing to the shallow

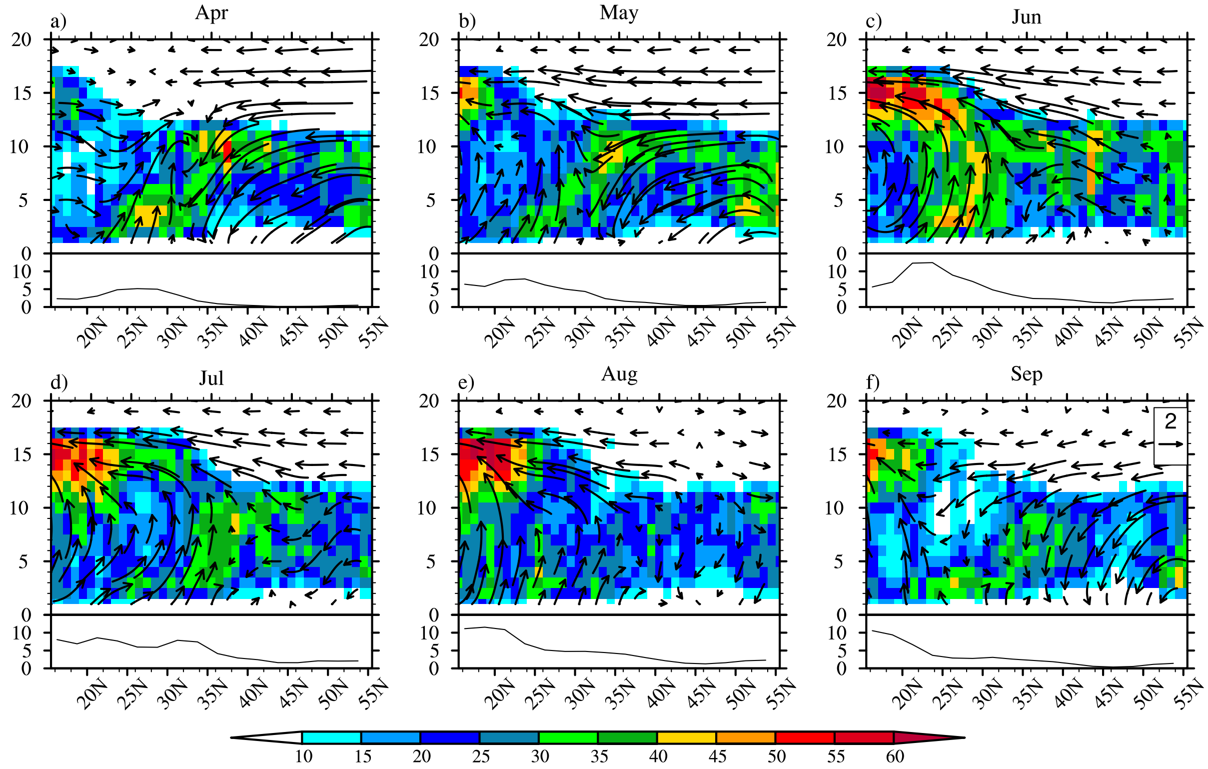

Fig. 4. The temporal evolution of height–latitude profiles of monthly mean CloudSat cloud occurrence frequency (shading) and meridional wind (vectors) over southeastern China (105°–120°E) from April to September (upper part in each panel), and the latitudinal profile of rainfall based on the same region (lower part in each panel) (units: mm d^{-1}; source: CMAP). The vertical coordinate is the height (units: km). The units of vectors are m s^{-1} (note the vertical velocity has been scaled).

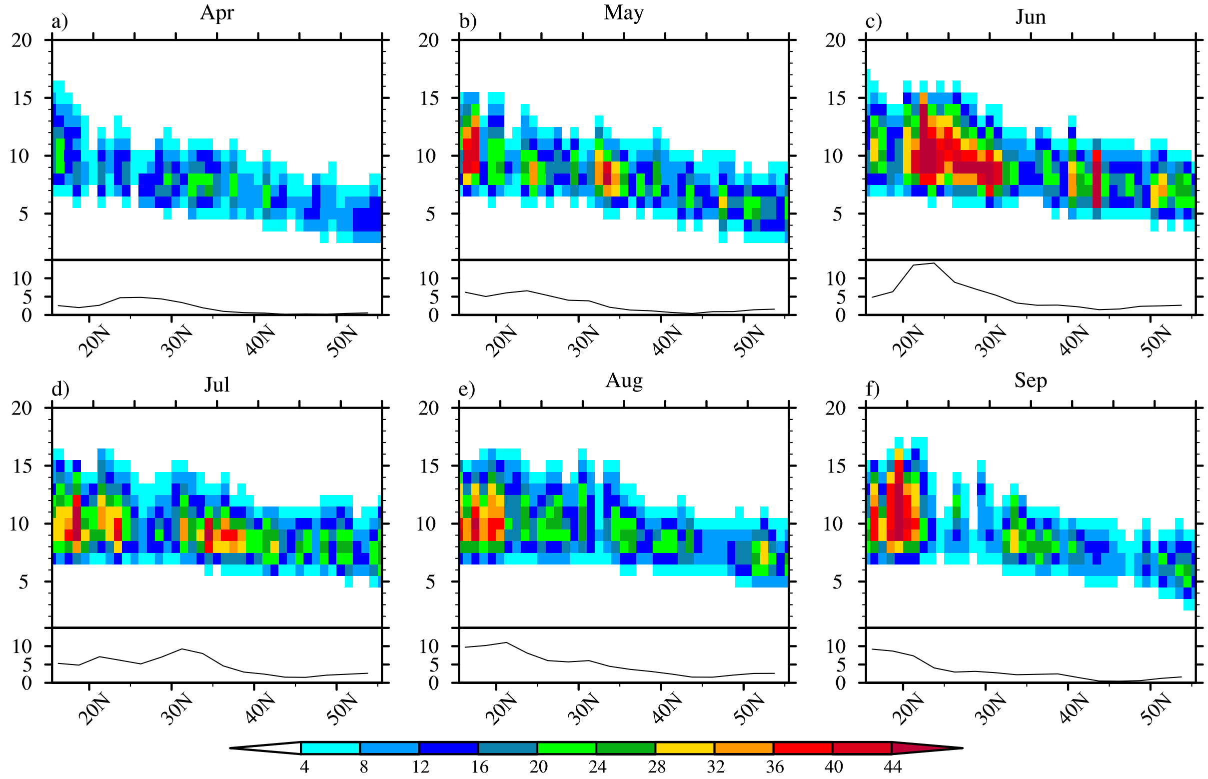

Fig. 5. The temporal evolution of height profiles of monthly mean CloudSat cloud ice water content over southeastern China (105°–120°E) from April to September (upper part in each panel) (units: mg m^{-3}), and the latitudinal profile of rainfall based on the same region (lower part in each panel) (units: mm d^{-1}; source: CMAP). The vertical coordinate is the height (units: km).

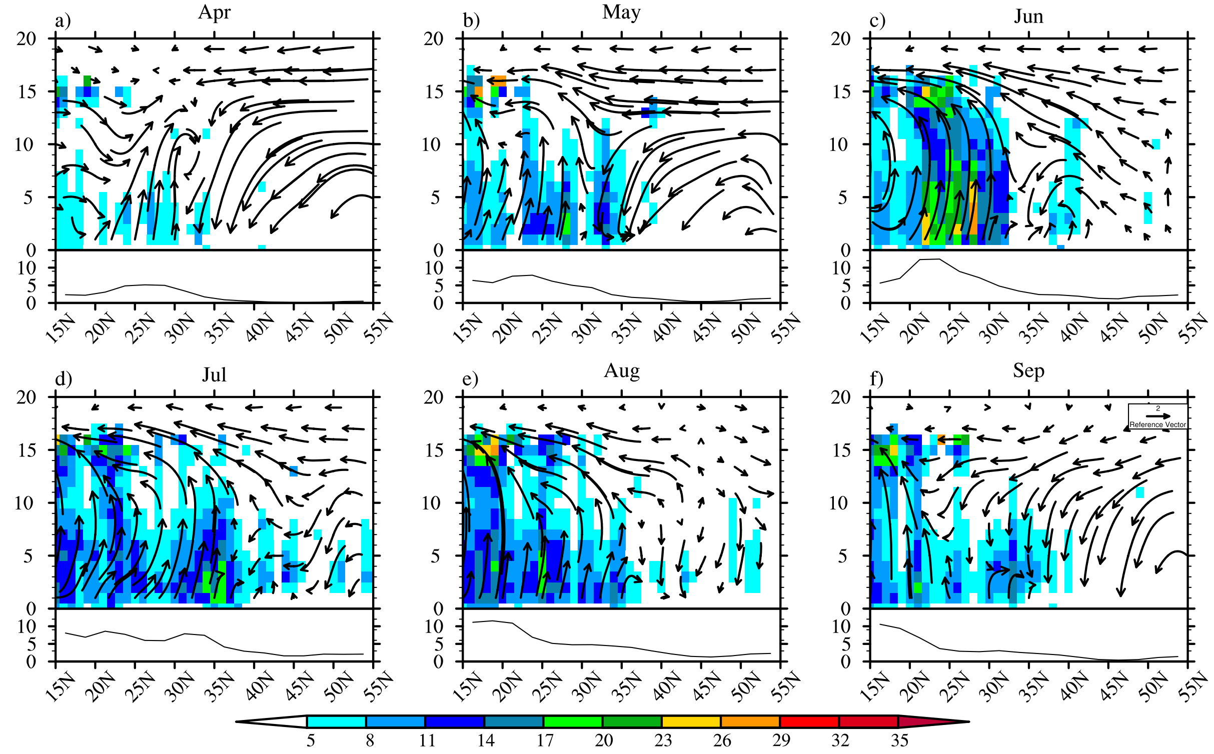

Fig. 6. The temporal evolution of height–latitude profiles of monthly mean CloudSat occurrence frequency of deep convective cloud over southeastern China (105°–120°E) from April to September (upper part in each panel), and the latitudinal profile of rainfall based on the same region (lower part in each panel) (units: mm d^{-1}; source: CMAP). The vertical coordinate is the height (units: km). The units of vectors are m s^{-1} (note the vertical velocity has been scaled).

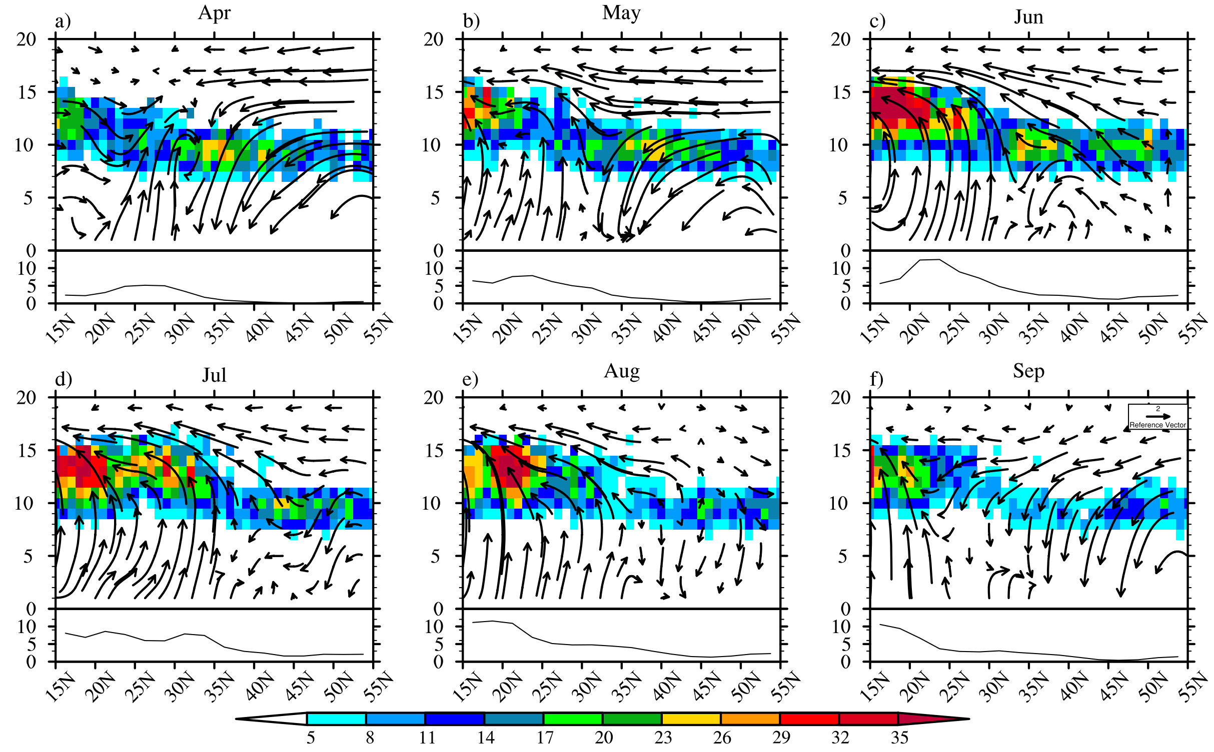

Fig. 7. The temporal evolution of height–latitude profiles of monthly mean CloudSat occurrence frequency of cirrus/cirrostratus cloud over southeastern China (105°–120°E) from April to September (upper part in each panel), and the latitudinal profile of rainfall based on the same region (lower part in each panel) (units: mm d^{-1}; source: CMAP). The vertical coordinate is the height (units: km). The units of vectors are m s^{-1} (note the vertical velocity has been scaled).

uplifts over the fronts, a large number of altostratus is found in front of the deep convective system. Following the northward march of deep convections in July, both the convective clouds and altostratus decrease sharply, but this kind of sharp transition is not evident in the amount of cirrus. Thus, the seasonal variation of cloud properties over southeastern China to a large extent reflects the seasonal march of monsoon circulation and the corresponding cloud system.

5. The radiative heating rates of clouds over southeastern China

The EASM is one of the most important triggers for the seasonal variation of general circulation and cloud types over southeastern China. Clouds can also influence the circulation through their radiative effects. To obtain information on cloud heating over southeastern China, the radiative heating rates (including longwave, shortwave, and net heating) for clear-sky and all-sky conditions are examined using CloudSat FLXHR data (Fig. 8). It should be noted that the clear-sky conditions are defined as the cloud mask value (GEOPROF product) equal to 0 (Mace, 2007). The vertical profile of radiative heating rates largely depends on the vertical distributions of absorbers or reflectors (e.g. moisture, clouds). In the following sub-sections, we discuss the clear-sky radiative heating rates and cloud effects over southeastern China.

5.1. *Clear-sky radiative heating rates*

The profile of longwave (LW) clear-sky cooling reflects the impact of water vapor and other greenhouse gases. In bo-

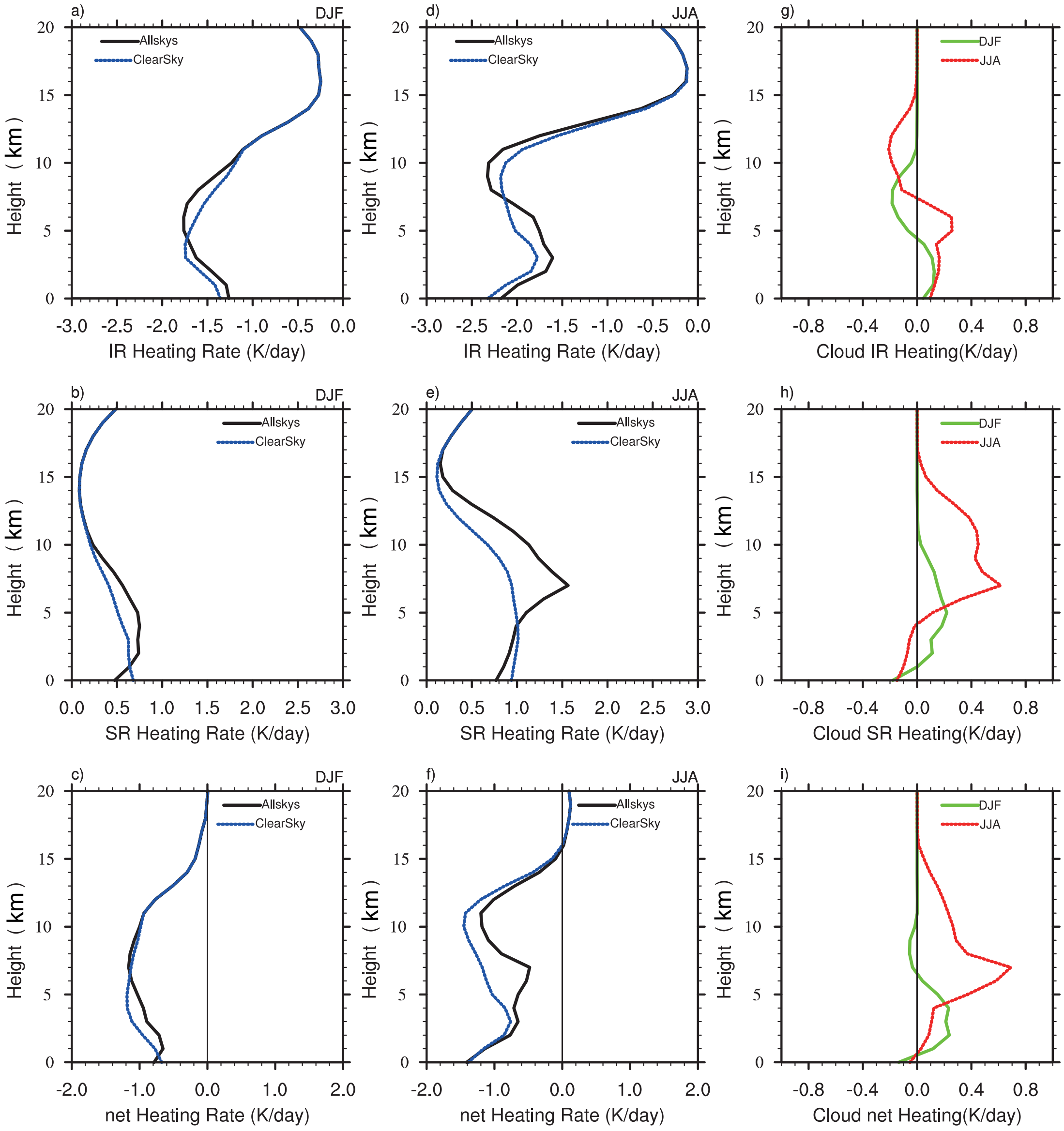

Fig. 8. Heating rates averaged over southeastern China (units: K d^{-1}): (a) Longwave heating rates for DJF (December–January–February); (b) shortwave heating rates for DJF; (c) net heating rates for DJF; (d–f) longwave, shortwave, and net heating rates for JJA (June–July–August), respectively; (g–i) cloud effects for both DJF and JJA (all-sky minus clear-sky).

real winter (Fig. 8a), the maximum LW cooling is located around 4–7 km, which corresponds to the maximum vertical gradient of moisture (Zhang and Chou, 1999). Because of the greenhouse effects of moisture, the boundary layer is usually opaque to LW flux. Thus, the LW cooling near the surface is small and increases with height up to 3 km, indicating a well-mixed boundary layer and a gradual reduction of moisture with altitude. The clear-sky LW cooling, which peaks at 4 km, tends to have a stabilizing effect on the high-level troposphere and thus restrains the vertical penetration of deep convections.

Over southeastern China, the wintertime SW clear-sky heating rate profiles show heating throughout the troposphere (Fig. 8b). Its distribution largely depends on the absorption of moisture and ozone (McFarlane et al., 2007). The vertical structure of SW heating reaches its maximum value at around 3–4 km, and then decreases with altitude. The magnitude of SW heating is smaller than that of LW. Thus, the net heating rate has a cooling effect in the troposphere, but turns to a heating effect above 15 km (Fig. 8c).

In summer, the moisture transport due to the monsoon results in a moist atmosphere, especially in the middle troposphere. Thus, the altitude of the maximum clear-sky LW cooling uplifts to 10 km, and then decreases sharply with height (Fig. 8d). They can also be found in the profiles of SW (Fig. 8e) and net heating (Fig. 8f). As the saturation vapor pressure is low at the high-level troposphere, the rapid decrease near 12 km might reflect CO_2 emissions and reduced water vapor emissions (Hartmann et al., 2001; Hartmann and Larson, 2002). The destabilizing effect of LW cooling extends to the mid-level, which is favorable for the occurrence of upward motion. Another extreme LW cooling (or SW heating) occurs near the surface (Fig. 5d–e), which might indicate a poorly-mixed boundary layer and is associated with decreased stratiform cloud.

The above evidence indicates that we can assume a positive feedback process between upward motion and the vertical profile of moisture. Following a strong deep convection, the vertical transport of moisture also increases, which favors the extension of LW cooling and enhances its destabilizing effect, reinforcing the uplifts, and finally leads to a moister upper troposphere.

5.2. *Cloud effects on radiative heating rates and its contribution to monsoon circulation*

Both the increase in high-cloud amounts and the height of clouds in summer are resulted from the deep convection associated with the development of the summer monsoon. The changed cloud properties can also influence the EASM circulation by changing the vertical profiles of radiative heating rates. The cloud radiative heating rates are generally defined as the difference between all-sky and clear-sky radiative heating rates (McFarlane et al., 2007; Mather et al., 2007). Figure 8 clearly reveals the seasonal difference in the vertical profiles of cloud radiative heating rates. The cloud warms the atmosphere by its greenhouse effect, and thus the atmosphere below the cloud layer is warmer than that of the clear sky (Fig. 8g). The cloud also influences the albedo and cools the atmosphere below the cloud. At the same time, the cloud absorbs solar radiative fluxes and heats the cloud top (Fig. 8h). In summer, following the increase in high clouds, the cloud LW heating also becomes stronger and the maximum value is evident at around 6–7 km, which is higher than in winter. Thus, the summertime high cloud serves as an additional heating source relative to the conditions of clear sky. It increases the vertical temperature gradient, which helps to maintain or even enhance the local atmospheric instability for upward motion.

Clouds also provide a stabilizing effect on the local atmosphere, as demonstrated by the SW heating rate (Fig. 8h). In summer, the reinforced deep convections increase the thickness of the cloud layer and the albedo is increased, which reflects more solar radiative flux and produces a cooling effect on the underlying cloud. The colder low-level atmosphere provides a stabilizing effect on the local atmosphere.

With regard to the climate mean conditions, the cloud heats the mid-troposphere over southeastern China in summer, as shown in Fig. 8i. Owing to the balance between heating and adiabatic cooling through upward motion, the above-mentioned cloud radiative heating further causes upward motions over southeastern China. Such a mechanism can be explained by the thermodynamic energy equation,

$$\frac{\partial T}{\partial t}+V\cdot\nabla T+w\frac{N^2H}{R}=Q\ . \tag{1}$$

This equation can be further simplified to

$$w\frac{N^2H}{R}=Q\ , \tag{2}$$

where T is the temperature, R is the gas constant, v/w is the horizontal/vertical velocity, H is the scale height, and Q are the heating rates. The Brunt–Vaisala frequency is defined by $N^2=(g/\theta)(\partial\theta/\partial z)$. Over southeastern China, the vertically averaged heating rate due to clouds is approximately 0.5 K d^{-1} in the troposphere. This indicates that the rate of ascent required to balance this additional cloud radiative heating is approximately -8 hPa d^{-1}, with its peak appearing at around 6–8 km, where the maximum cloud heating occurs (Fig. 9a). Actually, over southeastern China, the magnitude of summertime upward motion is about -20 hPa d^{-1} in the troposphere, as shown in Fig. 2. This indicates that the aggregate effect of cloud radiative heating has an important impact on local upward motion of the EASM circulation.

Such an additional rate of ascent associated with cloud radiative heating further affects the meridional wind by Sverdrup vorticity balances (Rodwell and Hoskins, 2001; Zhou et al., 2009b):

$$\beta v=f\frac{\partial\omega}{\partial p}\ , \tag{3}$$

where $f=2\Omega\sin\varphi$ is the Coriolis parameter and $\beta=2\Omega\cos\varphi/a$ is its meridional gradient. Based on the Sverdrup vorticity balance, the meridional wind is proportional to the vertical velocity gradient $\partial\omega/\partial p$ (Fig. 9b). Thus,

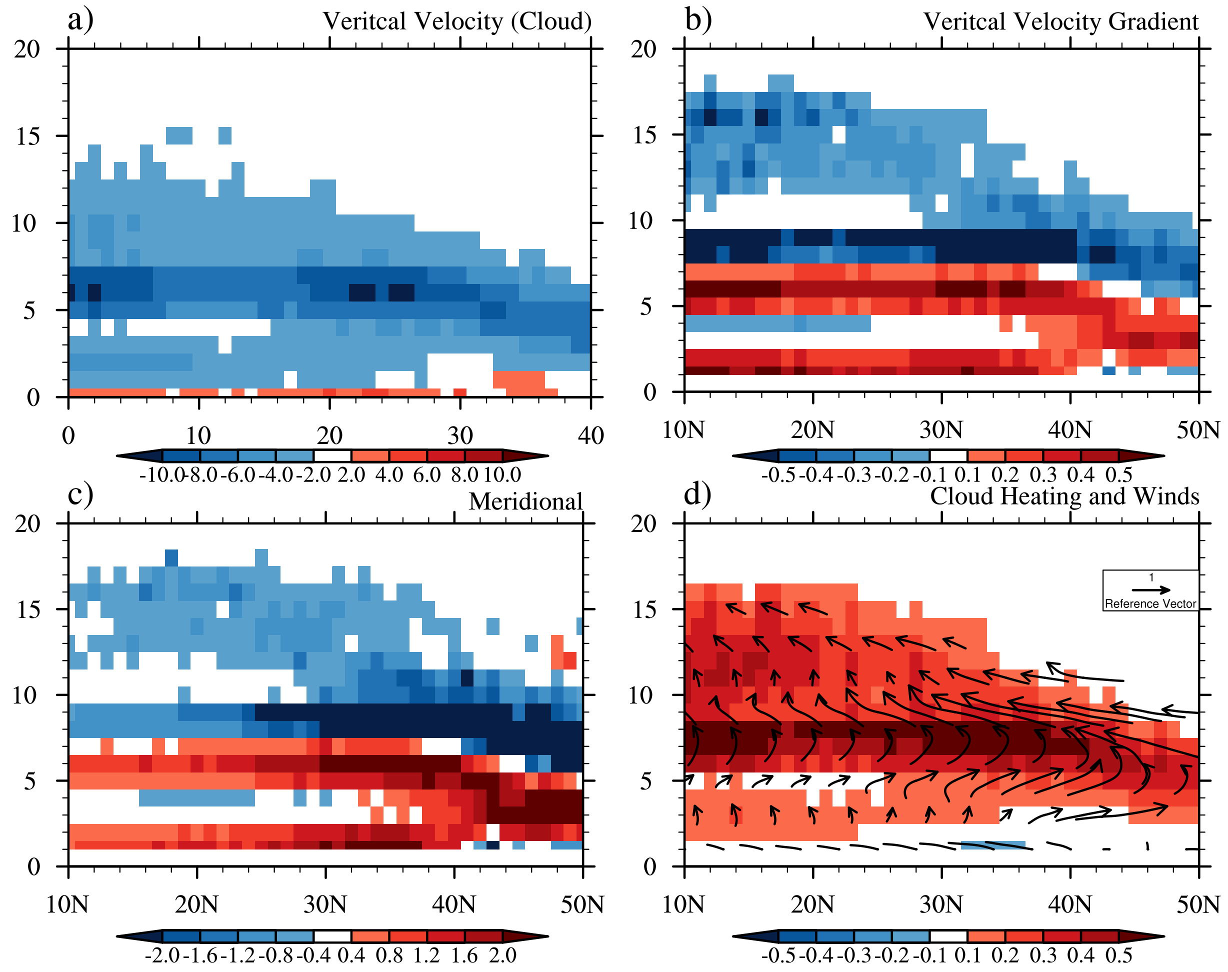

Fig. 9. Longitude–height cross section of (a) vertical velocity (ω, hPa d^{-1}), (b) vertical velocity gradient $\partial\omega/\partial p$, (c) meridional wind (m s^{-1}), and (d) cloud heating rates (shading) and cloud heating–forced wind [vectors, diagnosed based on Eqs. (4) and (5)] averaged from May to September. The vertical coordinate is the height (units: km). The units of vectors are m s^{-1} (note the vertical velocity has been scaled).

northerly wind prevails over the maximum center of $\partial\omega/\partial p$ while southerly wind appears below the maximum center of $\partial\omega/\partial p$ (Fig. 9c).

The cloud-forced upward motion and its resultant meridional wind constitute a meridional circulation (vectors in Fig. 10d) that coincides well with the EASM circulation (vectors in Fig. 4d). This indicates that the cloud-forced circulation has an important impact on the EASM circulation; there is positive interaction between cloud and the EASM circulation.

The radiative cooling that occurs in clear–sky conditions balances the convective heating and constrains the upwelling motions through large-scale circulations (Hartmann and Larson, 2002). Therefore, the vertical scale of the EASM circulation also depends on the local clear-sky radiative cooling profiles over southeastern China, although the cloud heating tends to enhance the EASM circulation.

The regional average of the clear-sky net radiative heating rate profile is observed to show a cooling throughout the troposphere in both the seasons (Figs. 8g–h). It is balanced by adiabatic heating through large-scale subsidence in clear–sky conditions and conforms to convective heating. Thus, maximum clear-sky radiative cooling occurs at altitudes with robust subsidence in clear-sky conditions and most convective clouds in cloudy conditions. Moreover, the strong decline in radiative cooling (both LW and net heating) with altitude is followed by strong convergence of mass at that level. The convergence is further balanced by the divergence of mass from convective regions. Thus, the high-frequency center of convective anvil or cirrus clouds occurs at this level, which is evident in Fig. 4 and Fig. 8, where large-scale meridional wind fields indicate a peak in convective detrainment and maximum divergence. Therefore, the altitude showing a strong decline in clear-sky net radiative cooling indicates the vertical scale of EASM upwelling or the top of convective cloud (Fig. 4).

In the above analysis, the latent heating is neglected for the purpose of assessing the impact of clouds. However, we note that the latent heating should not be ignored, especially at the lower level.

6. Conclusions

In this study, seasonal variations of cloud properties, occurrence frequency, and IWC of clouds over southeastern China were analyzed using CloudSat data. The seasonal cycle of cloud proprieties was explained based on the changes in monsoon circulations. The energy balance due to cloud heating was also investigated. The major results can be summarized as follows:

(1) The CloudSat data reveal a significant seasonal variation in cloud properties over southeastern China. Similar to ISCCP, the high and low clouds alternately dominate in CloudSat. Different from ISCCP, the prevailing cloud in winter is stratocumulus.

(2) The EASM is one of the most important triggers for the variations of cloud properties from winter to summer. The establishment of the EASM circulation and conditional instability caused by increased moisture result in frequent upward motions over southeastern China. Consequently, the high-cloud occurrence frequency increases sharply in summer. Moreover, the summertime weaker lower troposphere stability and stronger solar radiation reduce stratiform clouds in summer.

(3) Following the seasonal advance of the EASM circulation, the seasonal variations of deep convective clouds coincide well with those of the strongest upward motion and rain belt. The cirrus cloud always spreads outward from the convective systems, lags behind the rain belt, and coincides well with convective detrainment and maximum large-scale meridional wind divergence. The position of altostratus, which is caused by the front and uplifts flow, generally leads to the center of deep convective clouds.

(4) The vertical profiles of radiative heating rates show that both the moisture and clouds tend to destabilize the middle and lower troposphere, which is beneficial to the local upwelling. Clouds heat the underlying air by LW fluxes and their upper part by SW fluxes. Such a cloud radiative heating is required to be balanced by the rate of ascent, which further influences meridional wind through the Sverdrup vorticity balance. Circulation forced by cloud radiative heating coincides well with the EASM circulation, and is comparable to the EASM circulation in magnitude. Therefore, there is positive interaction between clouds and the EASM circulation because large-scale circulations connect clear-sky radiative cooling and cloudy-sky heating. The cloud distribution and vertical scale of the EASM circulation are also consistent with the profiles of clear-sky radiative heating. The strong decline in radiative cooling with altitude in clear-sky conditions is balanced by a strong divergence of mass with frequent convective anvil clouds, and the peak of clear-sky cooling is coupled with the convective cloud center.

Acknowledgements. This work was supported by the National Science Fund for Distinguished Young Scholars (41125017) and National Natural Science Funds of China (41405103).

REFERENCES

Arking, A., 1991: The radiative effects of clouds and their impact on climate. *Bull. Amer. Meteor. Soc.*, **72**, 795–813.

Cess, R. D., M. Zhang, B. A. Wielicki, D. F. Young, X.-L. Zhou, and Y. Nikitenko, 2001: The influence of 1998 El Niño upon cloud-radiative forcing over the Pacific warm pool. *J. Climate*, **14**, 2129–2137.

Chen, H., T. Zhou, R. B. Neale, X. Wu, and G. J. Zhang, 2010: Performance of the new NCAR CAM3.5 in East Asian summer monsoon simulations: Sensitivity to modifications of the convection scheme. *J. Climate*, **23**, 3657–3675.

Ding, Y., and J. C. L. Chan, 2005: The East Asian summer monsoon: An overview. *Meteor. Atmos. Phys.*, **89**, 117–142.

Hartmann, D. L., and K. Larson, 2002: An important constraint on tropical cloud–climate feedback. *Geophys. Res. Lett.*, **29**, doi: 10.1029/2002GL015835.

Hartmann, D. L., M. E. Ockert-Bell, and M. L. Michelsen, 1992: The effect of cloud type on Earth's energy balance: Global analysis. *J. Climate*, **5**, 1281–1304.

Hartmann, D. L., J. R. Holton, and Q. Fu, 2001: The heat balance of the tropical tropopause, cirrus, and stratospheric dehydration. *Geophys. Res. Lett.*, **28**, 1969–1972.

Houze, R. A., 1994: *Cloud Dynamics*. 2nd ed, Academic Press, San Diego, 573 pp.

Huang, B., and Z.-Z. Hu., 2007: Cloud–SST feedback in southeastern tropical Atlantic anomalous events. *J. Geophys. Res.*, **112**, doi: 10.1029/2006JC003626.

Kanamitsu, M., W. Ebisuzaki, J. Woollen, S.-K. Yang, J. J. Hnilo, M. Fiorino, and G. L. Potter, 2002: NCEP–DOE AMIP-II reanalysis (R-2). *Bull. Amer. Meteor. Soc.*, **83**, 1631–1643.

Klein, S. A., and D. L. Hartmann, 1993: The seasonal cycle of low stratiform clouds. *J. Climate*, **6**, 1587–1606.

L'Ecuyer, T. S., and J. H. Jiang, 2010: Touring the atmosphere aboard the A-Train. *Physics Today*, **63**(7), 36–41, doi: 10.1063/1.3463626.

L'Ecuyer, T. S., N. B. Wood, T. Haladay, G. L. Stephens, and P. W. Stackhouse Jr., 2008: Impact of clouds on atmospheric heating based on the R04 CloudSat fluxes and heating rates data set. *J. Geophys. Res.*, **113**, doi: 10.1029/2008JD009951.

Lin, W., M. Zhang, and N. G. Loeb, 2009: Seasonal variation of the physical properties of marine boundary layer clouds off the California coast. *J. Climate*, **22**, 2624–2638.

Luo, Y., R. Zhang, and H. Wang, 2009: Comparing occurrences and vertical structures of hydrometeors between eastern China and the Indian monsoon region using *CloudSat*/CALIPSO data. *J. Climate*, **22**, 1052–1064.

Mace, G., 2007: Level 2GEOPROF product process description and interface control document algorithm version 5.3. [Available online at http://www.cloudsat.cira.colostate.edu.]

Mace, G., and Coauthors, 2007: Level 2 Radar-Lidar GEOPROF Product Version 1.0 Process Description and Interface Control Document. JPL, Pasadena, USA, 1-20.

Mather, J. H., S. A. McFarlane, M. A. Miller, and K. L. Johnson, 2007: Cloud properties and associated radiative heating rates in the tropical western Pacific. *J. Geophys. Res.*, **112**, doi: 10.1029/2006JD007555.

McFarlane, S. A., J. H. Mather, and T. P. Ackerman, 2007: Analysis of tropical radiative heating profiles: A comparison of models and observations. *J. Geophys. Res.*, **112**(D14), doi: 10.1029/2006JD008290.

Norris, J. R., and C. B. Leovy, 1994: Interannual variability in stratiform cloudiness and sea surface temperature. *J. Climate.*, **7**(12), 1915–1925.

Rajeevan, M., and J. Sriviasan, 2000: Net cloud radiative forcing at the top of the atmosphere in the Asian monsoon region. *J. Climate*, **13**, 650–657.

Ramanathan, V., and W. Collins, 1991: Thermodynamic regulation of ocean warming by cirrus clouds deduced from observations of the 1987 El Niño. *Nature*, **315**, 27–32.

Rodwell, M. J., and B. J. Hoskins, 2001: Subtropical anticyclones and summer monsoons. *J. Climate*, **14**, 3192–3211.

Rossow, W. B. and R. A. Schiffer, 1991: ISCCP Cloud Data Products. *Bull. Amer. Meteor. Soc.*, 72, 2–20.

Sassen, K., and Z. Wang, 2008: Classifying clouds around the globe with the CloudSat radar: 1-year of results, *Geophys. Res. Lett.*, 35, L04805, doi:10.1029/2007GL032591.

Stephens, G. L., and Coauthors, 2002: The CloudSat mission and the A-train. *Bull. Amer. Meteor. Soc.*, **83**, 1771–1790.

Wang, B., I.-S. Kang, and J.-Y. Lee, 2004: Ensemble simulations of Asian–Australian monsoon variability by 11 AGCMs. *J. Climate*, **15**, 803–818.

Wang, W.-C., W. Gong, W.-S. Kau, C.-T. Chen, H.-H. Hsu, and C.-H. Tu, 2004: Characteristics of cloud radiation forcing over East China. *J .Climate*, **17**, 845–853.

Wang, Z., and K. Sassen, 2001: Cloud type and macrophysical property retrieval using multiple remote sensors. *J. Appl. Meteor.*, **40**, 1665–1682.

Wang, Z., and K. Sassen, cited 2007: Level 2 cloud scenario classification product process description and interface control document, version 5.0. [Available online at http://www.cloudsat.cira.colostate.edu.]

Xi, B., X. Dong, P. Minnis, and M. M. Khaiyer, 2010: A 10 year climatology of cloud cover and vertical distribution derived from both surface and GOES observations over the DOE ARM SGP site. *J. Geophys. Res.*, **115**(D12), doi: 10.1029/2009JD012800.

Xie, P., and P. A. Arkin, 1996: Analyses of global monthly precipitation using gauge observations, satellite estimates, and numerical model predictions. *J. Climate*, **9**, 840–858.

Ye, D. Z., and G. Yang, 1979: Mean meridional circulations over East Asia and the Pacific Ocean. I: Summer; II: Winter. *Sci. Atmos. Sinica*, **3**, 299–305. (in Chinese)

Yu, R., Y. Yu, and M. Zhang, 2001: Comparing cloud radiative properties between the eastern China and the Indian monsoon region. *Adv. Atmos. Sci.*, **18**, 1090–1102, doi: 10.1007/soo376-001-0025-1.

Yu, R., B. Wang, and T. Zhou, 2004: Climate effects of the deep continental stratus clouds generated by the Tibetan Plateau. *J. Climate.*, **17**(13), 2702–2713.

Zhang, C., and M.-D. Chou, 1999: Variability of water vapor, infrared radiative cooling, and atmospheric instability for deep convection in the equatorial western Pacific. *J. Atmos. Sci.*, **56**, 711–723.

Zhou, T., and Z. Li, 2002: Simulation of the East Asian summer monsoon using a variable resolution atmospheric GCM. *Climate Dyn.*, **19**(2), 167–180.

Zhou, T., B. Wu, and B. Wang, 2009a: How well do atmospheric general circulation models capture the leading modes of the interannual variability of the Asian–Australian monsoon? *J. Climate*, **22**, 1159–1173.

Zhou, T., and Coauthors, 2009b: Why the western Pacific subtropical high has extended westward since the late 1970s. *J. Climate*, **22**, 2199–2215.